Carbon felt electrodes for redox flow battery: Impact of compression on transport properties

Rupak Banerjee[a,*], Nico Bevilacqua[a], Arezou Mohseninia[b], Benjamin Wiedemann[b], Florian Wilhelm[b], Joachim Scholta[b], Roswitha Zeis[a,c]

[a] Karlsruhe Institute of Technology, Helmholtz Institute Ulm, Helmholtzstraße 11, 89081 Ulm, Germany
[b] Zentrum für Sonnenenergie- und Wasserstoff-Forschung, Helmholtzstraße 8, 89071 Ulm, Germany
[c] Karlsruhe Institute of Technology, Institute of Physical Chemistry, Fritz-Haber-Weg 2, 76131 Karlsruhe, Germany

ABSTRACT

In a flow battery setup, carbon felt materials are compressed to obtain higher performance from the battery. In this work, a commercially available carbon felt material, commonly used as electrodes in Vanadium Redox Flow Battery setups was evaluated for the transport properties (diffusivity, permeability, pressure drop required for maintaining flow, among others) while under seven set levels of compression, using an image analysis coupled with pore network modeling approach. X-ray computed tomography has been used to obtain the microstructure of a commercially available electrode under compressed conditions. An open-source pore network modeling tool, OpenPNM has been used to investigate the transport properties of the porous felt material at each of the set compression levels. The results from the modeling are compared against experimentally obtained electrolyte transport patterns visualized using synchrotron X-ray radiography. The electrical resistance of the carbon felt electrode was measured experimentally using a four-probe method. The compression resulted in a 58% reduction in permeability, and a 25% reduction in single-phase diffusion. This combination of ex-situ characterization of the electrical and fluid transport through the electrodes provides valuable data for modeling flow battery systems, and validating hypothesis from in situ testing.

1. Introduction

Redox flow batteries (RFBs) are an attractive option for grid-scale energy storage as they allow the energy capacity and the power density to be decoupled [1], thereby reducing the cost of installed energy storage capacities. A critical component of the RFBs is the carbon felt electrodes which provide the surface area for the reaction to occur. The structure of these electrodes is crucial to the operation as it defines the ease of flow of the electrolyte through the electrode, electrical conductivity, and structural stability [2]. Highly porous carbon felt materials have become the electrode of choice for RFB applications [3,4].

Gonzalez-Garcia et al. [5] presented an early study of the structural properties of carbon felt based porous media highlighting the need to investigating carbon felt based materials, using mercury porosimetry and reported the permeability, porosity, specific surface area, and the electrical resistivity of the material (RVC 4002 carbon felt from Le Carbone Lorraine) studied. One of the approaches used to improve the performance of the RFBs is to increase the compression of these carbon felt electrodes. Davies and Tummino [6] demonstrated that higher

performance could be extracted from Vanadium RFBs by compressing the felt electrodes to higher pressures. Their work was conducted on a carbon felt material from SGL Carbon (Meitingen, Germany), GFD 4.6EA. The authors showed that both the felt resistance and contact resistance of the felt electrodes decreased with increasing compression. They also demonstrated that the pressure required to pump the electrolyte through the electrode in a flow-through configuration increased linearly with compression. Research has also been done into decreasing the pressure required to pump the electrolyte by application of lubricant impregnated surfaces [7], and by the selection of other electrolytes [8]. Banerjee et al. [9] compared the pore space and the pressure required for saturating different electrode materials from two different manufacturers, including GFD 4.6EA from SGL Carbon.

Chang et al. [10] investigated the change in structure and electrical properties of carbon felt electrodes with an increase in compression, studying the effects of up to 40% compression. They demonstrated that the porosity decreases from over 80% to below 60% when subjected to a compression of 40%. They hypothesized that the large reduction in porosity was a cause for concern as the resistance to electrolyte flow

---

* Corresponding author.
  E-mail address: rupak.banerjee@kit.edu (R. Banerjee).

would increase significantly as a result. They also measured the electrical resistance and showed that the electrical resistance decreases rapidly with increase in compression, demonstrating a decrease in electrical resistance of up to 80% resulting from a compression of 40%. Oh et al. [11] used the morphological and electrical properties reported by Chang et al. [10] to develop a numerical model to predict the impact of compression on the energy efficiency of the Vanadium RFB, demonstrating that higher electrode compression resulted in higher energy efficiencies.

In a more recent work, Ghimire et al. [12] investigated the impact of compression of felt electrodes on the *in situ* performance of Vanadium RFBs. They demonstrated that with increasing compression the performance of these RFBs improved. However, when the compression was increased above 25 – 30%, the performance starts to decrease. This same trend was also observed in energy efficiency and discharge efficiencies. The authors also demonstrated that this *in situ* measured internal resistance also showed a decrease with increasing compression, demonstrating that the ex-situ results align with the *in situ* behavior.

Jervis et al. [13] investigated the impact of compression of carbon felt electrodes on their structural properties, using X-ray computed tomography measurements of a 4.6 mm thick carbon felt from SGL. The authors studied the compression up to 90% reduction in thickness; and demonstrated that the porosity decreased from over 90% to below 70%, and showed a non-linear decrease. They also showed that with the initial increases in compression, the volume-specific fiber surface area remained steady, however, a sudden reduction in the surface area was observed when the compression was increased to 90%.

X-ray computed tomography is a powerful tool to investigate the structural properties of the carbon felt electrodes. It has been used in several works to investigate carbon felt and carbon paper materials for redox flow [9,13] applications. It is often coupled with pore network modeling to investigate liquid or gas transport through porous materials [9,14–17].

In this study, a commercially available carbon felt electrode material is investigated for the impact of compression on the pore space characteristics and on the transport of the electrolyte through the electrode. The carbon felt is compressed to 7 levels of thickness and the structure is scanned using X-ray computed tomography. The resulting structure is converted to the equivalent pores space, and the transport properties of the electrode are simulated using an open-source pore network modeling approach. The simulation results have also been compared with experimentally obtained synchrotron X-ray radiography results as reported in a parallel study [18]. Electrical conductivity has also been measured and reported at each of the compression levels.

One goal of this study is to provide an insight into the impact that compression of electrodes has on the internal pore space. A well studied felt electrode has been investigated in this study in order to increase the applicability of the results as well as the ability to find other data which complements the understanding gained from this work. The new understanding gained from this study about the impacts of compression can be utilized in designing new felt electrode materials to perform better at a range of compression levels.

2. Methodology

In this work, a GFA 6EA carbon felt, from SIGRACELL battery electrodes (a division of SGL Carbon, Meitingen, Germany) was investigated. The sample was sequentially compressed by 67% (67% reduction in thickness) and X-ray computed tomograms (X-ray CT) were obtained at each set compression level, as shown in Table 1.

The compression was applied using a material testing stage MTS1 (Bruker Corp.). The electrode had an uncompressed thickness of 6 mm, and at maximum compression (67%) was reduced to a thickness of 2 mm. For the compression experiments, a circular sample of 10 mm diameter was measured. A segment of the image with a square cross-Section 2 mm of side length was taken from the center of the image for

Table 1
Compression parameters for the GFA 6.

Displacement (mm)	Sample thickness (mm)	Percentage compression (%)	Compressive pressure (kPa)
0	6.0	0	0
0.5	5.5	8.33	9
1.0	5.0	16.67	14
1.5	4.5	25.00	23
2.0	4.0	33.33	35
3.0	3.0	50.00	86
4.0	2.0	67.67	283

further analysis. The length 2 mm was selected as it provided a large enough sample to be representative of the felt material, as demonstrated by Fishman et al. [19] and George et al. [20]. Picking a larger sample subset would make the computation time longer without any added benefits. A 3 mm x 3 mm sample has $2.25\times$ the cross-sectional area, and for a fixed thickness, $2.25\times$ the volume. Therefore, there would significantly more pores and throats that would need to be computed without further improving the accuracy of the results significantly. Fig. 1 shows the tomograms as the compression is increased. Compression was applied by setting levels of displacement which resulted in the thickness being reduced by set values. The felt was allowed a relaxation time of 300 min between the application of compression and when the imaging was initiated to allow the material to stabilize. This was done to eliminate movement of the sample during the imaging, which would result in movement artifacts. Shorter relaxation times were not used based off prior testing experience.

The X-ray CT images were captured using a Skyscan 1172 desktop device at an energy level of 36 kV, and a source current of 222 μA. The images were captured at rotation angle steps of 0.2° and a spatial resolution of 3.17 μm/pixel. The radiographs were reconstructed to form the three-dimensional greyscale image stack providing information about the structure of the material. The reconstruction was conducted using NRECON® software (Bruker Corp.). The methodology applied for image acquisition and analysis is consistent with literature [9,17,21], for porous carbon materials being used in redox flow batteries as well as fuel cells.

The three-dimensional image obtained was binarized to identify the solid and void regions. This was achieved by applying a universal threshold to all of the samples and then using a median filter to eliminate any extra noise within the image. The process has been described in detail in earlier works [9,14,15]. The pore space was identified into a network of pores and throats using the SNOW algorithm developed by Gostick [22]. The SNOW algorithm is a watershed-based segmentation that identifies the pores based on the distance from the nearest solid phase. The network of pores and throats can then be used to calculate a variety of transport properties. Pore network models have been in use for simulating transport through porous materials since their introduction by Chatzis and Dullien [23] in 1977. One key advantage of using pore network models is the ability to simplify the porous structure and calculate transport properties at a lower computational cost. Pore network models have been used to successfully predict transport properties for cases with multiphase transport [24–27].

Transport properties such as permeability, single-phase diffusion, and invasion behavior within the porous media were calculated using the open-source pore network modeling framework OpenPNM [28,29], as has been described in detail in our earlier work [9]. The electrolyte was simulated to operate with a contact angle of 140° within the pores for the hydrophobic (untreated) felts, based on experimentally obtained values of surface contact angle [9]. For comparison with hydrophilic (activated) felts, a contact angle of 40° was simulated within the pores. Activated felts have been found to be hydrophilic [9]. OpenPNM was also used to understand the pathways followed by the electrolyte in
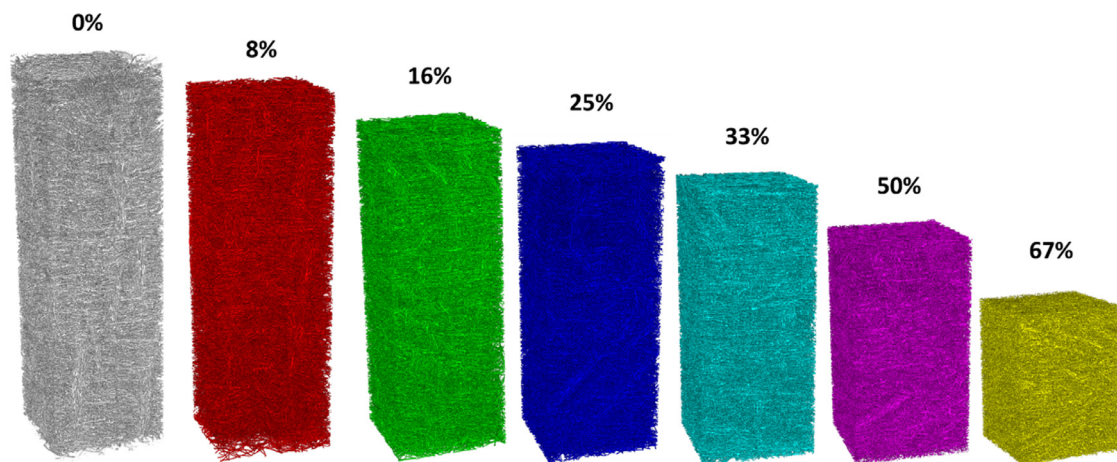
Fig. 1. Reconstructed tomograms of the compressed felt showing the change in thickness as the sample is compressed. The sample shown in the images has a side length of 2 mm, shown at compressions of (from left to right) 0%, 8%, 16%, 25%, 33%, 50%, and 67%.

navigating through the porous space of the electrode at different levels of compression. All the numerical results presented in this work, using OpenPNM, are steady-state results with no intention of the authors to imply any temporal resolution. This was also compared against experimental visualization results obtained using X-ray radiography conducted at the Karlsruhe Research Accelerator (KARA in Karlsruhe, Germany) at the Topo-Tomo beamline, presented in detail by Bevilacqua et al. [18].

The permeability of porous materials is a single-phase transport property, which defines the viscous transport resistance of fluid flow through the pores. It was obtained through the application of Darcy's law, where a pressure gradient was applied across the network of pores, resulting in the flow of the electrolyte. The flux of fluid flow across the network is calculated, and is used to calculate the permeability of the porous media and its equivalent pore network, using Darcy's formulation, as shown below:

$$K = \frac{Q}{A} \frac{\mu L}{\Delta P}$$

where K is the permeability of the porous network, Q is the volumetric rate of fluid flow, A is the cross-sectional area of the network, μ is the viscosity of the fluid, L is the thickness of the porous medium, and ΔP is the pressure difference applied across the network.

In the case of calculating single-phase diffusion through the network, Fick's law of diffusion is applied; such that a concentration of C_{inlet} is applied to one end of the network, and a concentration of C_{outlet} is applied to the other end, with L being the length of the network and A being the cross-sectional area. The flux of the diffusive component is measured across the network and represented as N, which can then be used to calculate the effective diffusion coefficient of the network using Fick's law of diffusion, as given below:

$$D = \frac{L \times N}{A \times (C_{inlet} - C_{outlet})}$$

Obtaining the invasion behavior of one fluid into the network, and displacing a defending fluid, involves a multi-phase interaction within the network. In this study, air is treated as the defending fluid, while the electrolyte is treated as the invading fluid. The pressure of the defending fluid is maintained at atmospheric pressure. The invading fluid is introduced at one face of the network at neutral pressure and the pressure is sequentially increased until the invading fluid enters into a pore within the network. As the pressure is further increased, more pores are sequentially filled which is tracked and can provide information into the resistance provided by the porous media for the invading phase to enter and saturated the medium. Additionally, this information can be used to predict the saturation of both the phases at

different pressures. The applicability of each of these transport properties is discussed in detail in an earlier work [9].

The X-ray radiography results presented in this work were collected at a mean energy of 13.5 keV, at a frame rate of 25 fps and a spatial resolution of 2.4 μm/pixel. The injection experiment was conducted using an injection device developed in-house, and used in earlier studies [17]. Injection experiments were conducted at different levels of compression to provide comparison points with the numerical study. The injection experiments are described in detail in a parallel study with a broad range of results relating to the impact of compression, impact of felt activation, and the impact of using different electrolytes [18].

Additionally, the through-plane electrical resistance was also measured at each of the set compression levels for the carbon felt electrode. For the electrical resistance measurement, the compression was applied using a Zwick/Roell Z005 universal testing machine. A sample with a diameter of 25 mm (circular cross-section) was obtained and the displacement was set. The resulting force was measured, which provided an insight into the compressive stresses being applied to the felt material. A relaxation time of 30 min was applied. A reduced relaxation time is used as the electrical resistance was continuously measured and it was observed that no further change in resistance was observed. Therefore, the reduced relaxation time was agreed upon. The electrical resistance was measured using a four-probe two-point method. A current of 1.0 A was applied through the sample and the resulting voltage was measured. The electrical resistance was calculated using Ohm's law. Table 1 shows the compressed sample thickness, percentage compression, and the compressive pressure at each level of displacement.

3. Repeatability and reproducibility

As presented, a number of processes are followed both in imaging the felt material, obtaining the equivalent pore network, and then calculating the individual transport properties. Some of these processes include the possibility of introducing uncertainty in the result, while others are deterministic and will not introduce any changes to the final result. In this section, the sources of uncertainty are discussed and their possible impact on the results are discussed.

The first step in this procedure is to compress the sample to the predetermined compression. A single sample is sequentially compressed to avoid variation in the starting thickness. The sample is compressed to set thicknesses which are 0.5 mm apart, while the device (MTS1 by Bruker Corp.) has an accuracy of 0.01 mm. The results are presented for the displacements such that the uncertainty in compression would not result in a significant change (<2%) in the compression.

The second step in this procedure is imaging the compressed sample using X-ray radiography and tomography. The imaging produces a greyscale image which includes a certain level of imaging noise. This quantification and mitigation of imaging noise have been studied for porous carbon materials [19,30–32], specifically for GDLs (in PEM fuel cells). However, the materials are similar, and the noise and error in these images are comparable. Fishman [31] introduced a methodology such that the GDL was considered to be present in images if at least 1% of the image was occupied by solid carbon of the GDL. Odaya et al. [32] also used this methodology in their work to study porous carbon materials. In a latter work, Banerjee et al. [21,33] utilized a modified methodology where the expected mass of the GDL was used as a method of calibrating the threshold for the images such that the density of the GDL was maintained in the images as compared to the GDL being measured. In this study, the latter methodology is utilized where a threshold is applied to the image to tune it against the expected mass of the GDL for the specified sample volume imaged. This allows the error in the image thresholding to be minimized.

The next step in the process is the extraction of the pore network, as described in the earlier section. This has been done using the algorithm presented by Gostick [22]. The uncertainty calculated by Gostick was lower than 2% for pores and less than 5% in the measurement of throats. This process of extracting the pore network creates the domain on which the simulations have been performed. Once the domain has been finalized, the process becomes deterministic as the pore network modeling algorithms operate on a pore by pore basis and therefore the pathways taken by the fluid is deterministic and finite. A change can be brought about by changing the inlet conditions, but those have been kept constant in this study. Therefore, no further sources of error arise in the calculation of the transport properties.

Considering the three sources of error described above, the root mean square error of the measurements arising from sequentially conducting these analyses is 3.46%. This is considered as the outer bounds of uncertainty for the measurements presented in this study, and is used as the error bounds in the data presented where applicable.

4. Results and discussion

Electrical resistance was measured in the carbon felt electrode sample at different levels of compression, and the results are presented in Fig. 2. Fig. 2(a) shows the electrical resistance as a function of the compression of the carbon felt. It was observed that the electrical resistance decreased linearly with increasing compression. Fig. 2(b) illustrates the electrical resistivity (specific electrical resistance) as a function of the compression of the felt. In this, it was observed that the resistivity decreases with increase in compression for the first 20% of

compression, beyond which it reaches an asymptotic value of approx. 8.4 mΩ·m. This suggests that the decrease in resistivity in the initial 20% compression arises from the increase in contact points as more of the surface fibers come in contact with the stamps, while the resistivity beyond this initial range does not change as there is no further change in the fundamental property of the material. The initial decrease in resistivity is attributed to improved contact and therefore lower contact resistance, while the asymptotic value of the resistivity is the property of the felt. This behavior of the resistivity reaching an asymptotic value has also been reported by Kossenko et al. [34].

A similar behavior was also presented by Chang et al. [10] with regard to the area-specific resistance of the carbon felts. Although they didn't present results for this type of felt, their study included both carbon felts as well as metal foam based felt materials. All these types of felt materials showed a similar behavior of decreasing resistance with compression to reach an asymptotic value. Gonzales-Garcia et al. [5] also presented their measurements of electrical resistivity of carbon felt materials, which was in the range of 10–16.3 mΩ m. In comparison, the results presented in this work, demonstrate the electrical resistivity of GFA6 ranges between 8–10 mΩ m and changes as a function of compression. The results of Gonzales-Garcia were for a different carbon felt material and therefore this level of variation is to be expected.

For the transport property calculations, a sample with a circular cross-section of 10 mm was cut and scanned at each of the same compression levels. Fig. 1 shows the tomograms of the compressed felt for each of the compressed states.

Fig. 3 shows the pore size distribution for the carbon felt electrode as it undergoes different levels of compression. The pore sizes are obtained directly after the pore space extraction using the SNOW algorithm [22], and the pore diameters have been binned into intervals of 5 μm. In Fig. 3(a), the total pore frequency is illustrated. As expected, the uncompressed sample has the largest number of pores and therefore has the largest pore frequencies. As the level of compression is increased the pore frequencies decrease at every pore diameter. The highest level of compression results in the lowest pore frequencies. In Fig. 3(b), the same information is presented as normalized pore frequency, where the pore frequency at each pore size is normalized by the total number of pores in the sample. As the sample is compressed, the total volume of pores decreases (as shown in Fig. 4), and therefore the normalized values show different trends. In the uncompressed sample, the normalized frequency distribution demonstrates a higher ratio of larger pores (pore diameters greater than 80 μm). The frequency of larger pores decreases as the level of compression is increased. This is complemented by the increase in smaller pores in the compressed felt as the larger pores collapse into smaller ones. In the range of 30–70 μm pore diameters, the uncompressed sample has a lower fraction of the
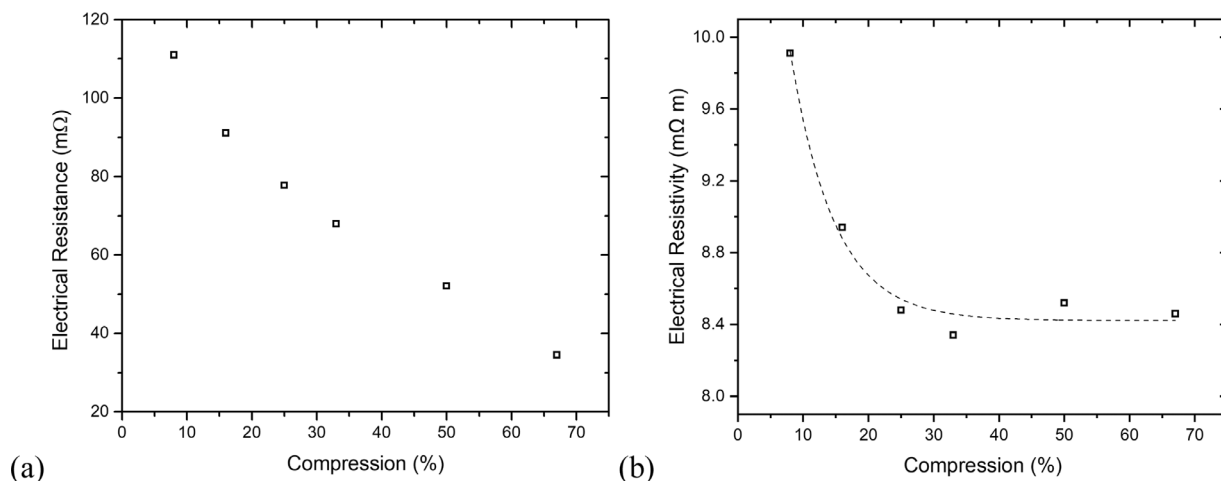

(a)

(b)

Fig. 2. (a) Electrical resistance, and (b) electrical resistivity as a function of compression for GFA 6, as measured directly.
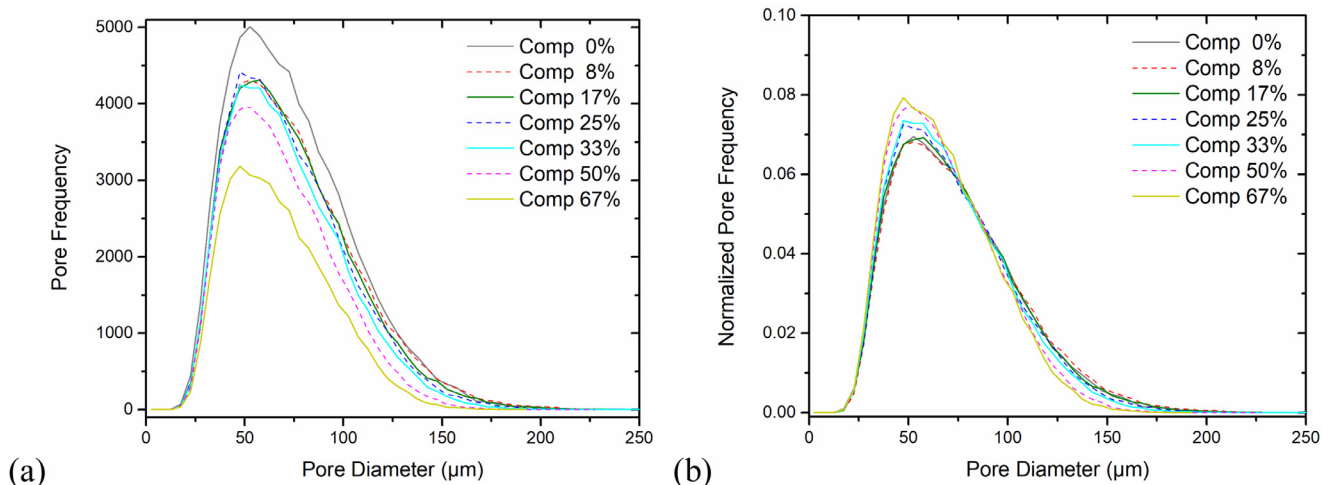
Fig. 3. Pore size distribution of the felt material as it is compressed to different levels. (a) absolute pore frequency (b) normalized pore frequency showing the ratios of pore sizes.

pores compared to the compressed sample. As the compression is increased, the percentage of pores in this range (30–70 μm) increases.

Fig. 4 illustrates the quantifiable changes in pore structure with an increase in compression. Fig. 4(a) shows the total pore volume per unit area of felt, which decreases with an increase in compression. The pore volume decreases linearly with compression and is reduced by up to 61% as the compression is increased to 67%. This is expected as the compression decreases the total volume and the solid volume of the fibers is unlikely to be reduced at these pressures, therefore, all the compression is taken up by the porous volume. Fig. 4(b) shows the mean pore diameters for the felt as compression is applied. Although the median pore diameter is close to 50 μm, the mean pore diameter is affected strongly by the distribution (shown in Fig. 3). The mean pore diameter for the uncompressed felt is about 74 μm, which becomes smaller with an increase in compression. This is attributed to the loss in large pores, as was observed in the pore size distribution shown in Fig. 3, and discussed above. As the large pores decrease in size, the decrease in mean pore diameter is non-linear, which is observed in Fig. 4(b). Fig. 4(c) illustrates the decrease in the maximum pore size in the felt as it is compressed. The graph shows that the maximum pore size decreases with an increase in compression, but does not follow a linear relationship. This is because the parameter depends on a single pore of that size within the domain and therefore can be affected by the changes in a sporadic fashion. This metric provides a clear comparison to the minimum capillary pressure required to get the electrolyte into the felt, although the pore may be located anywhere in the domain and therefore may not be accessible without first penetrating some smaller pores, with a higher entry capillary pressure.

The pore sizes of the carbon felt materials presented in this work is similar to the pore sizes reported in an earlier work by the authors [9,35] along with pore sizes for a similar carbon felt (GFD 4.6) presented by Jervis et al. [13]. The pore sizes for these carbon felt materials range from 2–200 μm throughout literature.

In order to understand the accessibility of the larger pores, the accessible volume of the felt at each pore diameter is presented in Fig. 5. On the horizontal axis is the pore diameter and the vertical axis represents the fraction of pore volume that is accessible by a spherical ball of the respective diameter. Using a small 1 μm spherical ball, 100% of the volume is accessible, while using a spherical ball of 250 μm, the porous space is not accessible at all. At pore diameters smaller than 50 μm, the effect of compression is not significant demonstrating that the small pores are not affected by the compression. The larger pores are impacted much more strongly and therefore using a spherical ball of 150 μm, only 2% of the pore volume is available at 67% compression

compared to 15% in the uncompressed case.

Fig. 6 shows the single-phase transport properties for the felt under the set levels of compression. Fig. 6(a) presents the permeability of the felt as a function of the compression applied. Permeability is calculated using Darcy's law after applying Stokes flow through the network of pores. A pressure difference of 101,325 Pa is applied across the two opposite faces of the porous network (101,325 Pa at the inlet face of the network, and 0 Pa at the outlet face of the network). The methodology is presented in greater detail in an earlier work [9]. The permeability of the uncompressed sample matches closely with literature, thereby validating the methodology [9,36]. It is observed that the permeability decreases with increase in compression. This is expected as the pores become smaller and therefore provide a larger resistance to the flow of the fluid through the network. Also shown in the figure, is the impact of compression on the transverse direction permeability. The permeability in the transverse direction is higher than the permeability in the normal direction of the felt. This is a similar behavior to similar material such as GDLs for PEM fuel cells, as shown by Gostick et al. [37]. However, the permeability in the transverse direction also followed the same trend with an increase in compression.

Fig. 6(b) presents the single-phase binary gas diffusion coefficient of air through the porous network of the felt, as a function of the compression. The effective diffusion coefficient is calculated by applying Fickian diffusion through the network of pores to obtain the effective diffusion coefficient of the porous media. There is a similar decrease in the effective diffusion coefficient of air through the sample with an increase in compression. As the sample is compressed by 67%, there is a decrease in the sample porosity resulting in a decrease in the single-phase binary diffusion coefficient. A decrease in the effective diffusion coefficient with a decrease in porosity is well established in literature for a variety of porous materials [38–41]. Fig. 6(c) presents the single-phase diffusion coefficient of water as a function of the increasing compression of the felt. The results show the same trend as the effective diffusion coefficient of air. The results for water would be expected to show similar trends to the diffusion coefficient of active reactant particles in the electrolyte, which is 0.1 M $VOSO_4$ in a 2 M solution of H_2SO_4, as the solution is an aqueous solution with vanadium and SO_4^{2-} ions [42,43]. The single phase effective diffusion coefficient reported in this work, matches closely with the effective diffusion calculated numerically [9] as well as experimentally obtained values for similar materials [40].

Fig. 7(a) presents the saturation curve for the felt electrodes at each level of compression. The imbibition process has been described in detail in an earlier work [9]. It is observed that the entry pressure for
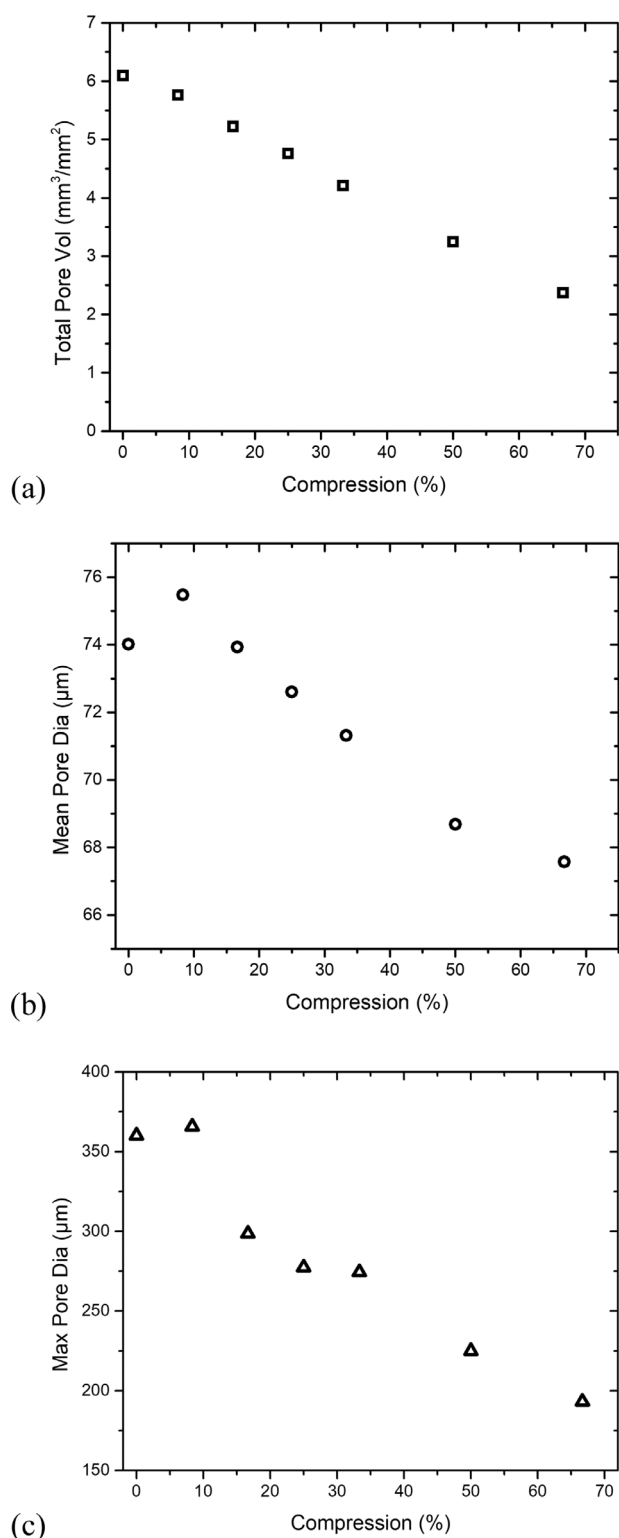
(a)

(b)

(c)

Fig. 4. Pore statistics quantifying the changes in pore structure with an increase in compression (a) total pore volume, (b) mean pore diameter, and (c) maximum pore size.

the fluid to enter the electrode rises with increased compression. The entry pressure depends on the larger pores available in the sample. With an increase in compression, the size of the largest pores decreases rapidly (see Fig. 4c), and therefore higher pressures are required for the pores in the electrode to be invaded. However, the pressure required to fully saturate the felts does not change as the smallest pores are not
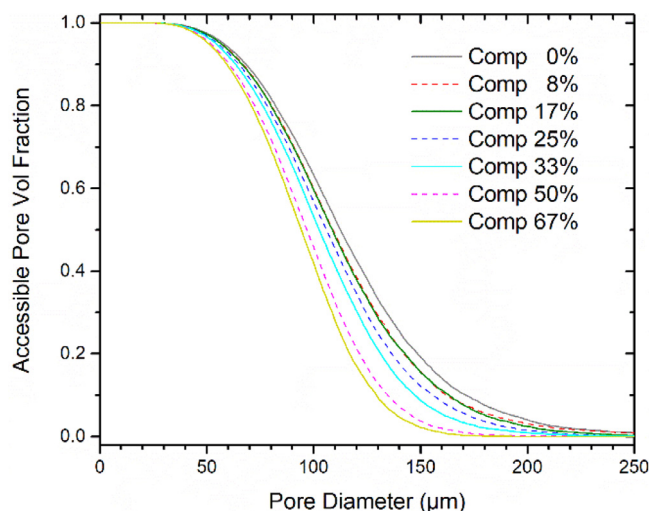

Fig. 5. Accessible pore volume as a function of pore diameter for the carbon felt at set levels of compression.

impacted by the increase in compression, as has been seen in Fig. 3. The breakthrough pressure for each of the conditions is shown in Fig. 7(b). It is observed that the breakthrough pressure shows a small dip at the lowest compression level, but thereafter demonstrates a linear increase in pressure with an increase in compression.

Table 2 presents a summary of the findings from Fig. 7 focusing on the applicability of this data to the RFB stack which is likely to be operated at certain pressures. Gundlapalli et al. [44] investigated the pressure drop in cells of different sizes and demonstrated that with a small cell size (100 cm^2), the pressure drop was lower than 2 kPa, while with a larger cell area of 414 cm^2, the pressure drop varied between 4–16 kPa. Assuming the outlet is maintained at atmospheric pressure (to maintain a high pump efficiency), the cell would be operated at the value of the pressure drop, *i.e.* between 2 and 16 kPa (as predicted by Gundlapalli et al. [44]). From Table 2, the saturation maintained at three different pressures in this range can be observed. At 5 kPa, the electrolyte has invaded the low compression electrodes (< 25% compression), while the highly compressed electrodes have not been invaded by the electrolyte. Even in the case of low compression electrodes, the saturation remains below 50%, therefore, this pressure is not suitable for the efficient operation of the VRFB. At 7 kPa, the electrolyte was able to invade into the felt electrode at each of the compression levels. However, with higher compression levels, the saturation decreased. The maximum saturation of 85% was obtained at 8% compression, while the minimum saturation of 33% was obtained at 67% compression level. At 10 kPa, the saturation was very similar as all the samples were nearly fully saturated (saturation > 96%). This illustrates that an operating pressure higher than the breakthrough pressure is necessary for any given compression level, while an operating pressure where the outlet is maintained at 10 kPa would enable the stack to operate at high saturation (and high surface utilization).

Fig. 8 shows the invasion pattern for each of the compression levels. For each of the figures, the invasion pattern is shown at the point of breakthrough, at which point there is a continuous pathway through the electrode and continuous operation can be sustained [9]. The colors of the invasion pattern correspond to the order in which the pores are invaded, which have been mapped to a blue to white colormap. Darker blues show the initial pores of invasion, while lighter blues and whites are the pores that are filled sequentially later. The lightest color on the map is mapped to the breakthrough location or the location at which invasion sequence ends.

From the figures, it is observed that the invasion pattern changes at each compression level as there is a change in the pore structure. The pores invaded can change with the change in the size of the pores at
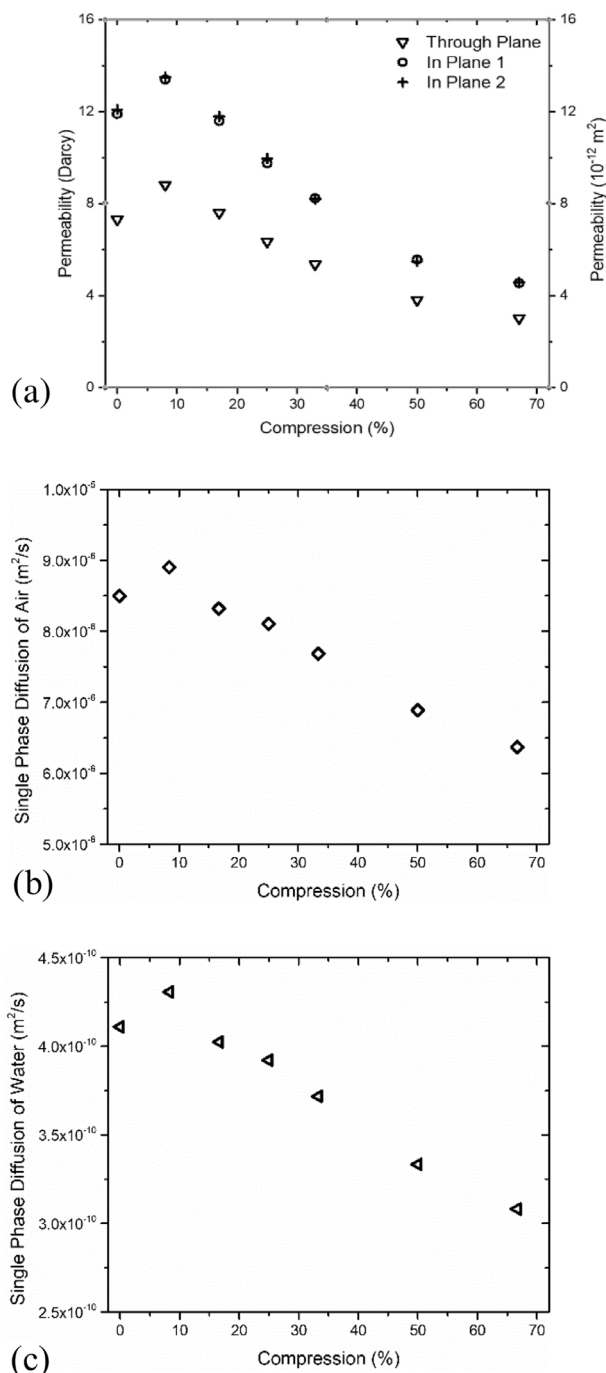
Fig. 6. Single phase transport parameters quantifying the changes in transport resistance with increase in compression (a) permeability, (b) single phase effective diffusion coefficient of air, and (c) single phase effective diffusion coefficient of water.

each invasion step. Additionally, the changes in the pattern are not linear and therefore cannot be predicted. This is true for most two-phase interactions [45,46]. The single-phase flow is much easily predicted while two-phase interactions require experimental or simulated experimental verification, as has been done here. A significant change in the invasion pattern can only be observed once the compression reaches 50%, as there is a significant decrease in the thickness and the pores are filled in a directional manner. In the cases of 25% and 33% compression, the invasion pattern shows a spreading of the liquid phase beyond the mid-section of the porous media. This is probably due to larger pores being connected which results in increased saturation in

that region. However, with increased compression (compression levels 50% and 67%), the larger pores collapse and therefore the pathway becomes more uni-directional, with the pores filling from the inlet to the breakthrough location, and results in reducing saturation with increasing distance from the inlet.

The local saturation of the electrodes is quantified and presented in Fig. 9. At each x-location (in the direction of electrolyte invasion) on the patterns in Fig. 8, the saturation is averaged in the y- and z-axis which is presented as the local saturation at that x-plane. At $x = = 0$, which is the inlet location, the saturation is 1, as all the pores are saturated. For each compression level, the maximum value of the through-plane position is different as the felt became increasingly compressed and therefore had reduced thicknesses in each progressive case. The maximum thickness was in the case of 0% compression, where the felt was 6 mm thick, while the lowest thickness was in the case of 67% compression, where the felt was reduced to a thickness of 2 mm. The value of saturation at the maximum through-plane location for each compression level decreased to very close to zero as this was the plane of breakthrough. From the saturation profiles, it was observed that at the highest compression level, the saturation decreases as the fluid moves along the x-axis and there is little fluctuation in the value of local saturation. However, in the case of the uncompressed sample, the saturation decreases in the initial entrance section, and then increases up to 40% saturation at several sections of the felt. As the felt is compressed, the fluctuations become less pronounced and very little fluctuations are observed at the compressions levels of 50%, and 67%. In the case of the felt compressed to 25%, a larger saturation is observed at the breakthrough point. This is explained by the volume of the pore that is filled at the time of breakthrough. If it is a small pore that is being invaded to reach the breakthrough point, the local saturation would remain low, which is the case for the other saturations, while in the case of 25% compression, a large pore may have been invaded, which results in a higher local saturation at the location of breakthrough.

Fig. 10 illustrates the invasion pattern exhibited by the invasion of water into the pore space of the compressed felt electrode at different times. It allows us to compare the modeling results with some experimental results obtained using water injection experiments [18] conducted on the same materials at the same compression state, and imaged using synchrotron X-ray radiography and tomography, as has been reported by Bevilacqua et al. [18]. This comparison focuses on the invasion from the point the electrolyte enters the porous media to the point of breakthrough. In Fig. 10(a), the results from the pore network model implemented in this study is shown, and a comparison can be drawn between the trends observed and the results shown by Bevilacqua et al. [18] as shown in Fig. 10(b). As the network model does not account for flow velocity, which the experimental observations depend on, the breakthrough time is matched between the two studies and the intermediate steps are calculated as fractions of the pores invaded, normalized against the breakthrough time. From this figure, it can be observed that the invasion patterns exhibit similar behavior and invasion depth is very similar in both the experimental and numerical scenarios. There are patterns of capillary fingering that can be observed in both invasion sequences which show that the electrolyte is seeking pathways ahead of the advancing liquid phase front.

Fig. 11 illustrates the comparison between the invasion patterns into a hydrophobic felt and a hydrophilic felt, as observed experimentally (using synchrotron X-ray radiography) and numerically (using OpenPNM). In both cases, it was observed that a significantly higher saturation of electrolyte was achieved with hydrophilic conditions in the felt, compared to hydrophobic conditions. This is an expected result, but demonstrates the ability of the numerical tool to accurately predict trends in electrolyte invasion in the porous electrode. The hydrophobic case in Fig. 11(b) shows low saturations, which is a function of it being hydrophobic as well as the image thresholding, which has been kept the same as the hydrophilic case, for consistency. The low thresholding to avoid image saturation in the case of hydrophilic case
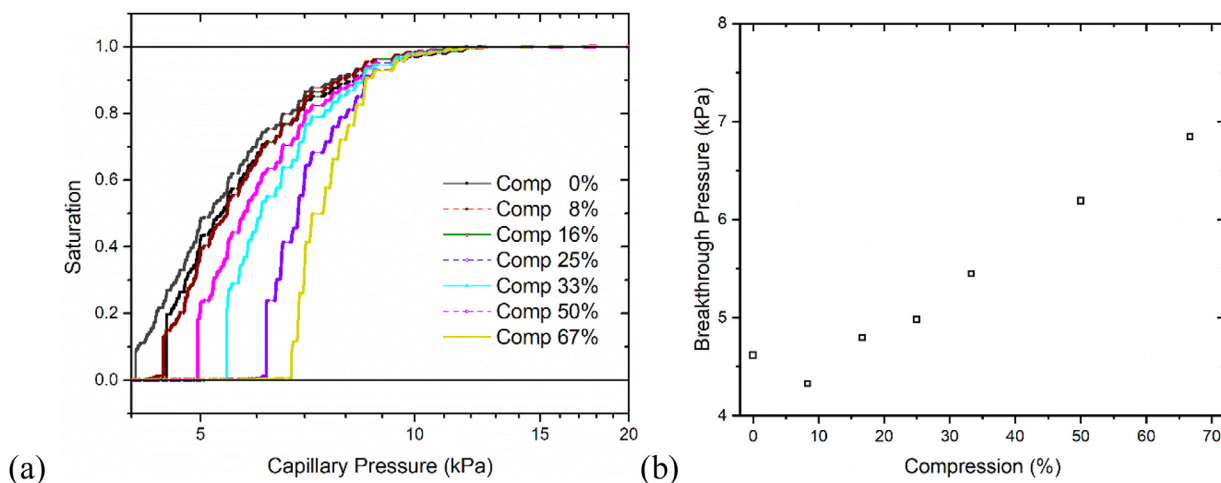
Fig. 7. (a) Imbibition curve for water invading the felt material under set levels of compression. The felt is modeled in its non-activated state where the material is treated as hydrophobic (CA = 140°). (b) Breakthrough saturation and breakthrough pressure for the felt material at each of the compression levels.

Table 2
Saturation of the compressed felt electrodes at different operating pressures.

Compression (%)	Saturation		
	At 5 kPa	At 7 kPa	At 10 kPa
0	0.42	0.82	0.97
8	0.48	0.85	0.98
17	0.38	0.83	0.98
25	0.22	0.79	0.98
33	0.00	0.74	0.98
50	0.00	0.60	0.97
67	0.00	0.33	0.97

means the hydrophobic case seems to be lower.

Each of these two techniques have their advantages. While it is easier to invade the hydrophilic felt with the electrolyte and image it, working with the hydrophobic conditions is impeded by the high pressures involved and the tendencies for leakage pathways to open up. Therefore, the modeling approach is more suitable for the hydrophobic material and the trends in saturation and transport properties can be captured with ease in this case. Additionally, the edge effects are another instance that can be captured using the modeling effort while the experimental approach results in the liquid transport being affected by the walls.
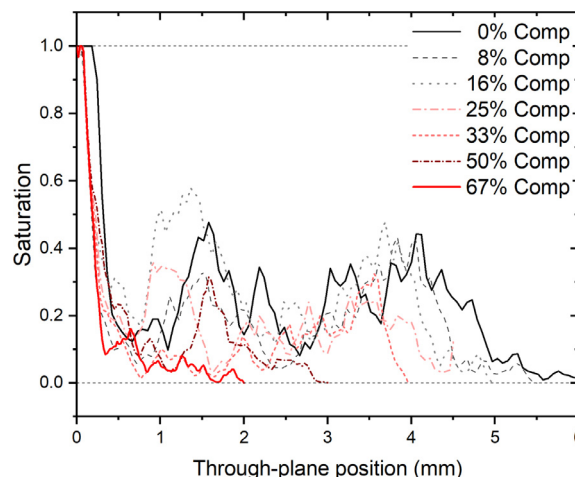

Fig. 9. Local saturation at each compression level, quantifying the saturation visualized in Fig. 8.

5. Discussion

The results presented in this work should be used to understand the impact of compression on the morphological and transport properties of
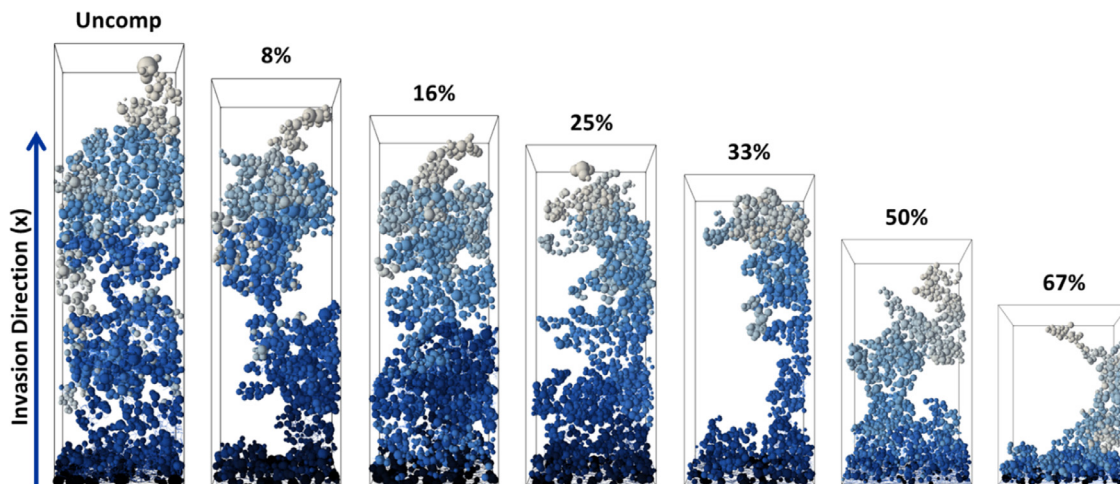

Fig. 8. Invasion patterns for the electrolyte moving through the porous network of the electrode until it reaches breakthrough on the opposite face.
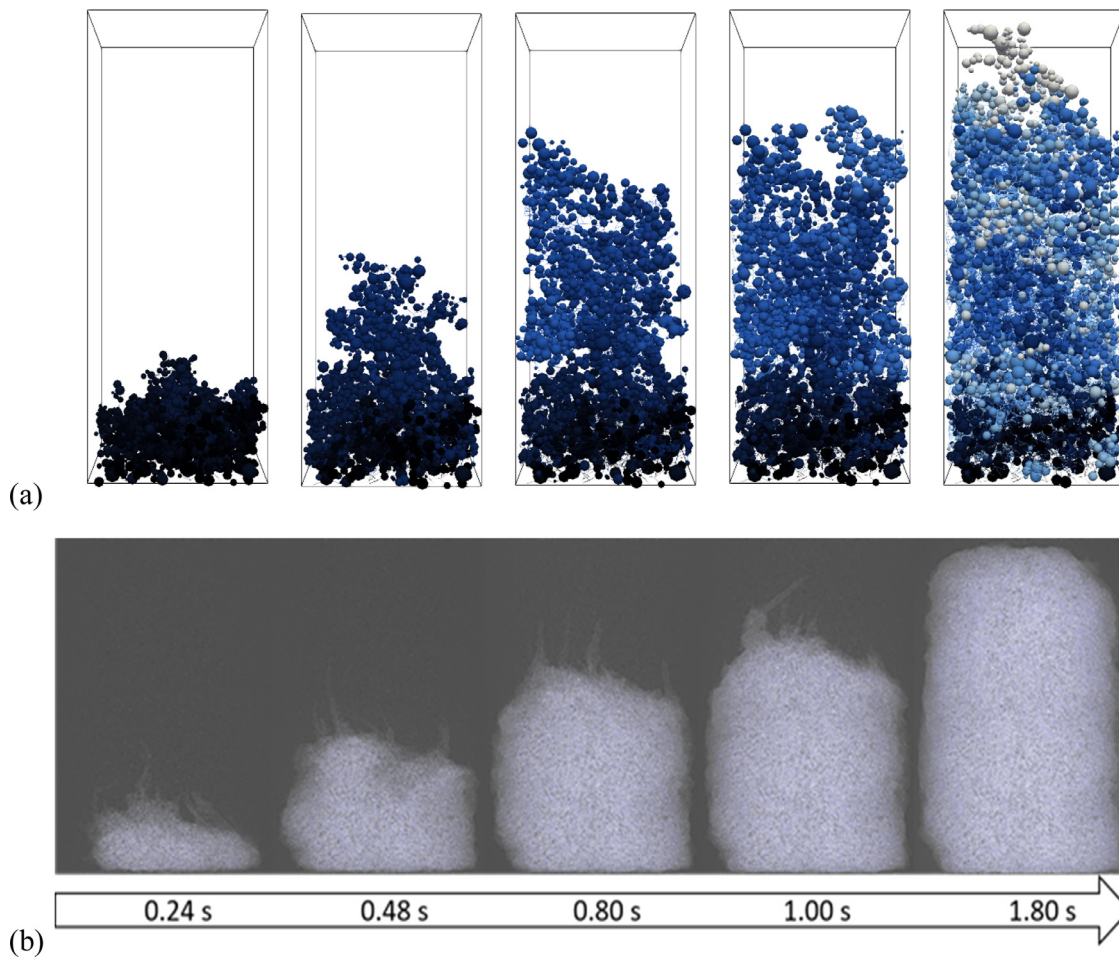
Fig. 10. Electrolyte invasion process in a hydrophilic (activated) felt material at a compression rate of 25% (reduction in thickness) (a) as simulated in OpenPNM, and (b) as imaged using synchrotron X-ray radiography and reported by Bevilacqua et al. [18].

the carbon felt electrode being studied here. The data does match up with the trends observed and reported earlier in literature. However, the data should not be focused upon in isolation, as experimental conditions such as uneven pressure distribution on felt electrodes, localized large pores, or preferential transport pathways among other variabilities may cause the actual experimental result to differ from the modeling domain and thus create results that are slightly different.

In this work, the pore size distribution result showed an unexpected increase in the medium to large-sized pores in the case where the felt electrode was compressed to 8% compression. The maximum pore sizes
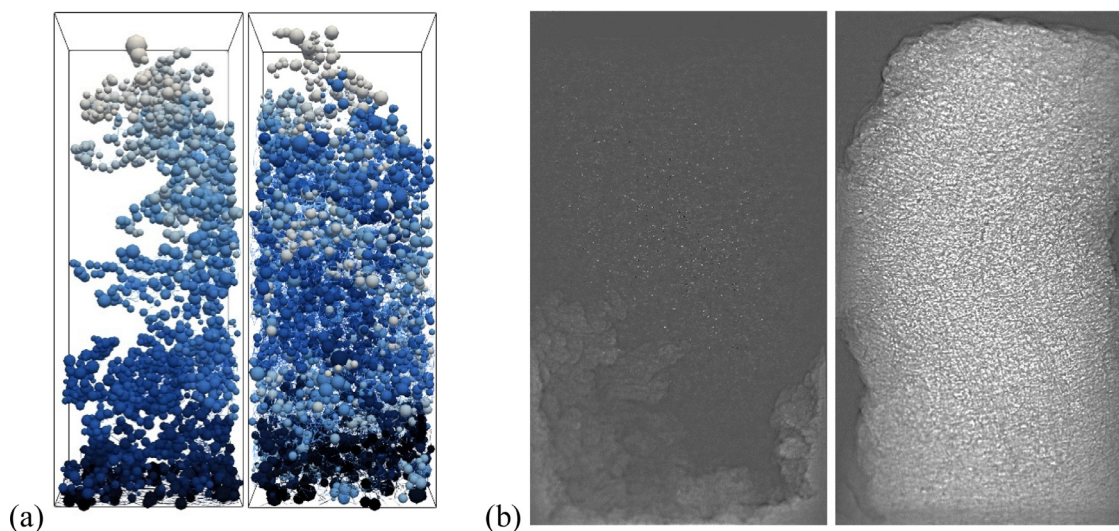

Fig. 11. Comparison water invasion patterns of hydrophobic (Contact angle = =140°) and hydrophilic (Contact angle = =40°) felt materials as observed in (a) OpenPNM, and (b) synchrotron X-ray radiography and reported by Bevilacqua et al. [18].

increased by only 1.6%, while the mean pore size increased by 2.0%. However, this change leads to an unexpected increase in the transport properties that have been calculated throughout the work. The unexpected result obtained for 8% compressed electrode should be treated as an anomaly. The invasion patterns and the saturation were less influenced by the anomalous behavior at 8% compression, as the patterns of increasing breakthrough pressure and decreasing overall saturation were maintained at that level of compression.

Overall, it was observed that increasing compression resulted in smaller pores, and therefore higher transport resistances for electrolyte transport. Viscous transport through the electrode was reduced to a larger degree, as the permeability decreased by about 59% as a result of the 67% compression, whereas diffusive transport decreased by only 25% resulting from the same level of compression. Therefore, processes which rely on diffusive transport are less likely to see an increase in transport resistance, compared to processes which depend on viscous transport.

Changes in transport properties have a strong impact on the electrochemical processes of the VRFBs. Increased compression has shown to decrease porosity and increase permeability. Increased permeability results in a higher pressure drop when the VRFB is operated in flow-through mode, which leads to higher pumping losses and thus lower overall efficiencies. [47,48]. The effective diffusion coefficient provides a measure of the diffusive transport resistance of the porous material. The diffusive transport within the electrodes of the VRFB arises from the transport of active ions (V2+, V3+, V4+, V5+) within the electrolyte. As the reaction progresses, the continued redistribution of the active ions minimizes the transport resistance and associated losses. Diffusive transport affects the transport of the active ions from the bulk of the electrolyte to the localized reaction sites.

The breakthrough pressure, presented as a metric in this work, allows us to understand the ease with which the electrolyte would be able to traverse through the electrode structure. The breakthrough pressure combined with the imbibition curve, and the saturation information provides us with a picture of how the electrolyte invades the pore space of the electrode. In this case, it is observed that with increased compression, the breakthrough pressure increased, which indicates that a higher pressure is required to get the electrolyte from one face of the electrode to the other. If the VRFB is operated in a flow-by mode this would be the minimum pressure required to get the electrolyte to reach the membrane, such that operation of the RFB could be started. In a flow-through mode, the breakthrough pressure would be the minimum pressure required to establish a continuous pathway of electrolyte through the electrode, and sustain continuous operation. The imbibition curve shows the continuous relationship between the invasion pressure and saturation. It is observed that the compressive pressure defines the pressure at which the electrode can begin to be saturated. However, the pressure at which the electrode becomes fully saturated, is independent of the compressive pressure. This is because the full saturation is dictated by the smallest pores in the electrode, which do not change significantly with an increase in compression.

In summary, the goal of this work is to present an understanding of the impact of compression on the pore space of carbon felt electrodes. A general electrode, which is commonly studied is used to enhance the impact of the study, as it can be coupled with other studies to gain greater insight. Other investigations into a variety of felt electrode materials have resulted in similar trend lines being drawn which illustrate that the results are not standalone and can be extrapolated to other materials. Although it is not the author's intent to suggest that all designers need to conduct the same type of analysis on all their materials, however, the study does provide information on what the impact of compression is on the pore space of felt electrodes. This can be used to design materials which will perform better under higher compression levels.

6. Conclusions

In this study, a commercially available carbon felt electrode designed for use in redox flow batteries by SGL has been investigated for the impact of compression on the electrical resistivity, and the single-phase and multi-phase fluid flow. A GFA 6 carbon felt, with a nominal thickness of 6 mm, was compressed to set levels of up to 67% compression (67% reduction in thickness). The electrical resistance was observed to decrease linearly, while the electrical resistivity decreased during the first 20% compression, thereafter reaching an asymptotic value. The single-phase transport parameters were also calculated through the porous network, and it was demonstrated that the compression resulted in a 58% reduction in permeability, 25% reduction in single-phase diffusion, and the accessible pore volume at a diameter of 150 μm decreased from 15% to 2% of the total porous volume.

Additionally, as part of this work, the electrolyte was simulated to invade the electrolyte and the entrance capillary pressure to start the saturation process increased from 4.5 kPa to over 6.5 kPa. The invasion patterns and the local saturation were also presented, demonstrating fewer fluctuations in the local saturation with an increase in compression. This was attributed to the reduction in pore sizes throughout the sample. The breakthrough saturation decreased slightly, and the breakthrough pressure increased by 48% as a result of the compression.

Through this work, it was demonstrated that the pressure required for the flow to be maintained and the entrance pressures increase significantly at higher levels of compression. However, the pressure required to fully saturate the sample does not increase. The permeability decreases with increased compression, which results in higher pumping power losses if operated in a flow-through configuration. These transport parameters need to be calculated and compared for different levels of compression during the optimization process to decide the compression pressure at which the flow battery should be operated. In addition, trends observed in this study were compared with experimentally observed saturation and invasion pathways, as obtained using synchrotron X-ray radiography to compare the experimental and numerical observations. As the electrical resistance decreases linearly, and the pumping pressure losses increase linearly with increasing compression, an optimum point needs to be found where the benefits of both can be leveraged. This would best be explored using *in situ* studies at the different compression levels and through system modeling approaches which can account for the electrolyte flow as well as the electrical resistance, and electrical heat generation in a system.

Declaration of Competing Interest

None.

Supplementary materials

Supplementary material associated with this article can be found, in the online version, at doi:10.1016/j.est.2019.100997.

References

[1] A.Z. Weber, M.M. Mench, J.P. Meyers, P.N. Ross, J.T. Gostick, Q. Liu, Redox flow batteries: a review, J. Appl. Electrochem. 41 (2011) 1137, https://doi.org/10.1007/s10800-011-0348-2.

[2] C. Minke, U. Kunz, T. Turek, Carbon felt and carbon fiber - a techno-economic assessment of felt electrodes for redox flow battery applications, J. Power Sources 342 (2017) 116–124, https://doi.org/10.1016/j.jpowsour.2016.12.039.

[3] V. Haddadi-Asl, M. Kazacos, M. Skyllas-Kazacos, Carbon–polymer composite electrodes for redox cells, J. Appl. Polym. Sci. 57 (1995) 1455–1463, https://doi.org/10.1002/app.1995.070571205.

[4] J.-Z. Chen, W.-Y. Liao, W.-Y. Hsieh, C.-C. Hsu, Y.-S. Chen, All-vanadium redox flow batteries with graphite felt electrodes treated by atmospheric pressure plasma jets, J. Power Sources 274 (2015) 894–898, https://doi.org/10.1016/j.jpowsour.2014.10.097.

[5] J. González-García, P. Bonete, E. Expósito, V. Montiel, A. Aldaz, R. Torregrosa-Maciá, Characterization of a carbon felt electrode: structural and physical properties, J. Mater. Chem. 9 (1999) 419–426, https://doi.org/10.1039/a805823g.

[6] T.J. Davies, J.J. Tummino, High-Performance Vanadium redox flow batteries with graphite felt electrodes, C. 4 (2018) 8, https://doi.org/10.3390/c4010008.

[7] B.R. Solomon, X. Chen, L. Rapoport, A. Helal, G.H. McKinley, Y.-.M. Chiang, K.K. Varanasi, Enhancing the performance of viscous electrode-based flow batteries using lubricant-impregnated surfaces, ACS Appl. Energy Mater. (2018), https://doi.org/10.1021/acsaem.8b00241.

[8] A. Mukhopadhyay, J. Hamel, R. Katahira, H. Zhu, Metal-free aqueous flow battery with novel ultrafiltered lignin as electrolyte, ACS Sustain. Chem. Eng. 6 (2018) 5394–5400, https://doi.org/10.1021/acssuschemeng.8b00221.

[9] R. Banerjee, N. Bevilacqua, L. Eifert, R. Zeis, Characterization of carbon felt electrodes for vanadium redox flow batteries – a pore network modeling approach, J. Energy Storage 21 (2019) 163–171, https://doi.org/10.1016/j.est.2018.11.014.

[10] T.-.C. Chang, J.-.P. Zhang, Y.-.K. Fuh, Electrical, mechanical and morphological properties of compressed carbon felt electrodes in vanadium redox flow battery, J. Power Sources 245 (2014) 66–75, https://doi.org/10.1016/j.jpowsour.2013.06.018.

[11] K. Oh, S. Won, H. Ju, Numerical study of the effects of carbon felt electrode compression in all-vanadium redox flow batteries, Electrochimica. Acta. 181 (2015) 13–23, https://doi.org/10.1016/j.electacta.2015.02.212.

[12] P.C. Ghimire, A. Bhattarai, R. Schweiss, G.G. Scherer, N. Wai, Q. Yan, A comprehensive study of electrode compression effects in all vanadium redox flow batteries including locally resolved measurements, Appl. Energy 230 (2018) 974–982, https://doi.org/10.1016/j.apenergy.2018.09.049.

[13] R. Jervis, M.D.R. Kok, T.P. Neville, Q. Meyer, L.D. Brown, F. Iacoviello, J.T. Gostick, D.J.L. Brett, P.R. Shearing, In situ compression and X-ray computed tomography of flow battery electrodes, J. Energy Chem. (2018), https://doi.org/10.1016/j.jechem.2018.03.022.

[14] M.D.R. Kok, R. Jervis, P.R. Shearing, J.T. Gostick, Fluid transport properties from 3D tomographic images of electrospun carbon electrodes for flow batteries, ECS Trans. 77 (2017) 129–143, https://doi.org/10.1149/07711.0129ecst.

[15] M. Fazeli, J. Hinebaugh, A. Bazylak, Investigating inlet condition effects on PEMFC GDL liquid water transport through pore network modeling, J. Electrochem. Soc. 162 (2015) F661–F668, https://doi.org/10.1149/2.0191507jes.

[16] E.F. Medici, I.V. Zenyuk, D.Y. Parkinson, A.Z. Weber, J.S. Allen, Understanding water transport in polymer electrolyte fuel cells using coupled continuum and pore-network models, Fuel Cells 16 (2016) 725–733, https://doi.org/10.1002/fuce.201500213.

[17] N. Bevilacqua, M.G. George, S. Galbiati, A. Bazylak, R. Zeis, Phosphoric acid invasion in high temperature PEM fuel cell gas diffusion layers, Electrochimica. Acta. 257 (2017) 89–98, https://doi.org/10.1016/j.electacta.2017.10.054.

[18] N. Bevilacqua, L. Eifert, R. Banerjee, K. Köble, T. Faragó, M. Zuber, A. Bazylak, R. Zeis, Visualization of electrolyte flow in vanadium redox flow batteries using synchrotron X-ray radiography and tomography—Impact of electrolyte species and electrode compression, J. Power Sources 439 (2019) 227071, , https://doi.org/10.1016/j.jpowsour.2019.227071.

[19] Z. Fishman, J. Hinebaugh, A. Bazylak, Microscale tomography investigations of heterogeneous porosity distributions of PEMFC GDLs, J. Electrochem. Soc. 157 (2010) B1643–B1650, https://doi.org/10.1149/1.3481443.

[20] M. George, Z. Fishman, S. Botelho, A. Bazylak, Micro-computed tomography-based profilometry for characterizing the surface roughness of microporous layer-coated polymer electrolyte membrane fuel cell gas diffusion layers, J. Electrochem. Soc. 163 (2016) F832–F841, https://doi.org/10.1149/2.0531608jes.

[21] R. Banerjee, J. Hinebaugh, H. Liu, R. Yip, N. Ge, A. Bazylak, Heterogeneous porosity distributions of polymer electrolyte membrane fuel cell gas diffusion layer materials with rib-channel compression, Int. J. Hydrog. Energy 41 (2016) 14885–14896, https://doi.org/10.1016/j.ijhydene.2016.06.147.

[22] J.T. Gostick, Versatile and efficient pore network extraction method using marker-based watershed segmentation, Phys. Rev. E. 96 (2017) 023307, , https://doi.org/10.1103/PhysRevE.96.023307.

[23] I. Chatzis, F.A.L. Dullien, Modelling pore structure by 2-D and 3-D networks with applicationto sandstones, J. Can. Pet. Technol. 16 (1977), https://doi.org/10.2118/77-01-09.

[24] T.G. Tranter, J.T. Gostick, A.D. Burns, W.F. Gale, Pore network modeling of compressed fuel cell components with OpenPNM, Fuel Cells 16 (2016) 504–515, https://doi.org/10.1002/fuce.201500168.

[25] M. Fazeli, J. Hinebaugh, A. Bazylak, Incorporating embedded microporous layers into topologically equivalent pore network models for oxygen diffusivity calculations in polymer electrolyte membrane fuel cell gas diffusion layers, Electrochimica. Acta. 216 (2016) 364–375, https://doi.org/10.1016/j.electacta.2016.08.126.

[26] A.K.C. Wong, R. Banerjee, A. Bazylak, Tuning MPL intrusion to increase oxygen transport in dry and partially saturated polymer electrolyte membrane fuel cell gas diffusion layers, J. Electrochem. Soc. 166 (2019) F3009–F3019, https://doi.org/10.1149/2.0021907jes.

[27] J.T. Gostick, M.A. Ioannidis, M.W. Fowler, M.D. Pritzker, Pore network modeling of fibrous gas diffusion layers for polymer electrolyte membrane fuel cells, J. Power Sources 173 (1) (2007) 277–290, https://doi.org/10.1016/j.jpowsour.2007.04.059.

[28] A. Putz, J. Hinebaugh, M. Aghighi, H. Day, A. Bazylak, J.T. Gostick, Introducing OpenPNM: an open source pore network modeling software package, ECS Trans. 58 (2013) 79–86, https://doi.org/10.1149/05801.0079ecst.

[29] J. Gostick, M. Aghighi, J. Hinebaugh, T. Tranter, M.A. Hoeh, H. Day, B. Spellacy, M.H. Sharqawy, A. Bazylak, A. Burns, W. Lehnert, A. Putz, OpenPNM: a pore network modeling package, Comput. Sci. Eng. 18 (2016) 60–74, https://doi.org/10.1109/MCSE.2016.49.

[30] M.G. George, X-ray-based Imaging for Characterizing Heterogeneous Gas Diffusion Layers for Polymer Electrolyte Membrane Fuel Cells, University of Toronto (Canada), 2016.

[31] Z. Fishman, A. Bazylak, Heterogeneous through-plane porosity distributions for treated PEMFC GDLs I. PTFE effect, J. Electrochem. Soc. 158 (8) (2011) B841–B845, https://doi.org/10.1149/1.3594578.

[32] S. Odaya, R.K. Phillips, Y. Sharma, J. Bellerive, A.B. Phillion, M. Hoorfar, X-ray tomographic analysis of porosity distributions in gas diffusion layers of proton exchange membrane fuel cells, Electrochimica. Acta. 152 (2015) 464–472, https://doi.org/10.1016/j.electacta.2014.11.143.

[33] R. Banerjee, S. Chevalier, H. Liu, J. Lee, R. Yip, K. Han, B.K. Hong, A. Bazylak, A comparison of felt-type and paper-type gas diffusion layers for polymer electrolyte membrane fuel cell applications using X-Ray techniques, J. Electrochem. Energy Convers. Storage. 15 (2018) 011002, , https://doi.org/10.1115/1.4037766.

[34] A. Kossenko, S. Lugovskoy, M. Averbukh, Electric and hydraulic properties of carbon felt immersed in different dielectric liquids, Materials 11 (2018) 650, https://doi.org/10.3390/ma11040650.

[35] A. Fetyan, J. Schneider, M. Schnucklake, G.A. El-Nagar, R. Banerjee, N. Bevilacqua, R. Zeis, C. Roth, Comparison of electrospun carbon−carbon composite and commercial felt for their activity and electrolyte utilization in vanadium redox flow batteries, ChemElectroChem. 6 (2019) 130–135, https://doi.org/10.1002/celc.201801128.

[36] T. Jyothi Latha, S. Jayanti, Ex-situ experimental studies on serpentine flow field design for redox flow battery systems, J. Power Sources 248 (2014) 140–146, https://doi.org/10.1016/j.jpowsour.2013.09.084.

[37] J.T. Gostick, M.W. Fowler, M.D. Pritzker, M.A. Ioannidis, L.M. Behra, In-plane and through-plane gas permeability of carbon fiber electrode backing layers, J. Power Sources 162 (2006) 228–238.

[38] D.A.G. Bruggeman, Berechnung verschiedener physikalischer Konstanten von heterogenen Substanzen. I. Dielektrizitätskonstanten und Leitfähigkeiten der Mischkörper aus isotropen Substanzen, Ann. Phys. 416 (1935) 665–679.

[39] R. Flückiger, S.A. Freunberger, D. Kramer, A. Wokaun, G.G. Scherer, F.N. Büchi, Anisotropic, effective diffusivity of porous gas diffusion layer materials for PEFC, Electrochimica. Acta. 54 (2008) 551–559.

[40] J.M. LaManna, S.G. Kandlikar, Determination of effective water vapor diffusion coefficient in pemfc gas diffusion layers, Int. J. Hydrog. Energy 36 (2011) 5021–5029, https://doi.org/10.1016/j.ijhydene.2011.01.036.

[41] D. Muirhead, R. Banerjee, M.G. George, N. Ge, P. Shrestha, H. Liu, J. Lee, A. Bazylak, Liquid water saturation and oxygen transport resistance in polymer electrolyte membrane fuel cell gas diffusion layers, Electrochimica. Acta. (2018), https://doi.org/10.1016/j.electacta.2018.04.050.

[42] L. Eifert, R. Banerjee, Z. Jusys, R. Zeis, Characterization of carbon felt electrodes for vanadium redox flow batteries: impact of treatment methods, J. Electrochem. Soc. 165 (11) (2018) A2577–A2586, https://doi.org/10.1149/2.0531811jes.

[43] L. Eifert, Z. Jusys, R. Banerjee, R.J. Behm, R. Zeis, Differential electrochemical mass spectrometry of carbon felt electrodes for vanadium redox flow batteries, ACS Appl. Energy Mater. 1 (2018) 6714–6718, https://doi.org/10.1021/acsaem.8b01550.

[44] R. Gundlapalli, S. Kumar, S. Jayanti, Stack design considerations for vanadium redox flow battery, INAE Lett. 3 (2018) 149–157, https://doi.org/10.1007/s41403-018-0044-1.

[45] R. Banerjee, S.G. Kandlikar, Liquid water quantification in the cathode side gas channels of a proton exchange membrane fuel cell through two-phase flow visualization, J. Power Sources 247 (2014) 9–19, https://doi.org/10.1016/j.jpowsour.2013.08.016.

[46] R. Banerjee, D. Howe, V. Mejia, S.G. Kandlikar, Experimental validation of two-phase pressure drop multiplier as a diagnostic tool for characterizing PEM fuel cell performance, Int. J. Hydrog. Energy 39 (2014) 17791–17801, https://doi.org/10.1016/j.ijhydene.2014.08.118.

[47] J. Houser, A. Pezeshki, J.T. Clement, D. Aaron, M.M. Mench, Architecture for improved mass transport and system performance in redox flow batteries, J. Power Sources 351 (2017) 96–105, https://doi.org/10.1016/j.jpowsour.2017.03.083.

[48] Q. Xu, T.S. Zhao, C. Zhang, Performance of a vanadium redox flow battery with and without flow fields, Electrochimica. Acta. 142 (2014) 61–67, https://doi.org/10.1016/j.electacta.2014.07.059.